

## Revision 1

# Structural behavior and magnetic properties of coquimbite $\text{AlFe}^{3+}_3(\text{SO}_4)_6(\text{H}_2\text{O})_{12}\cdot 6\text{H}_2\text{O}$ over a wide temperature range

Word count 7503

Veronika R. Abdulina<sup>1</sup>, Artem S. Borisov<sup>2</sup>, Oleg I. Siidra<sup>1,3\*</sup>, Victoria A. Ginga<sup>4</sup>, Nicolas Sanchez<sup>4</sup>, Annette Setzer<sup>4</sup>, Astrid Holzheid<sup>2</sup>

<sup>1</sup> Department of Crystallography, St. Petersburg State University, University Embankment 7/9,  
199034 St. Petersburg, Russia

<sup>2</sup> Institut für Geowissenschaften der Universität Kiel, Olshausenstr. 40, D-24098 Kiel, Germany

<sup>3</sup> Kola Science Center, Russian Academy of Sciences, Apatity 184200, Murmansk Region,  
Russia

<sup>4</sup> Felix Bloch Institute for Solid-State Physics, Leipzig University, Linnestrasse 5, 04103 Leipzig,  
Germany

\*E-mail: [o.siidra@spbu.ru](mailto:o.siidra@spbu.ru)

## Abstract

Hydrated iron sulfate minerals receive considerable attention from the standpoint of environmental science, and also due to extensive studies of the mineralogy of Mars. In this paper, we report on the thermal evolution of coquimbite  $\text{AlFe}^{3+}_3(\text{SO}_4)_6(\text{H}_2\text{O})_{12}\cdot 6\text{H}_2\text{O}$  by single-crystal X-ray diffraction (SCXRD) in the range of  $-173$  to  $77$  °C. Powder X-ray diffraction (PXRD) was performed in the temperature range of  $-180$  to  $740$  °C and low vacuum of 600 Pa. Magnetic properties for coquimbite are reported in the range of  $-271$  °C to  $7$  °C. It was observed that

coquimbite is stable between  $-180\text{ }^{\circ}\text{C}$  and  $+145\text{ }^{\circ}\text{C}$  and low vacuum of 600 Pa. We observed a gradual transition from coquimbite to the amorphous phase at  $150\text{ }^{\circ}\text{C}$ , followed by a transition to mikasaite at  $225\text{ }^{\circ}\text{C}$ , and a second amorphization at  $575\text{ }^{\circ}\text{C}$ , with afterward crystallization to hematite. SCXRD shows that the behavior of coquimbite with increasing temperature can be divided into two stages, with negative and strongly anisotropic thermal expansion at Stage I ( $-173$  to  $-143\text{ }^{\circ}\text{C}$ ) and only positive thermal expansion at Stage II ( $-133\text{ }^{\circ}\text{C}$  to  $77\text{ }^{\circ}\text{C}$ ). All the O–H $\cdots$ O bonds remain virtually intact during the Stage I except for Ow2–H3 $\cdots$ O2. The negative thermal expansion observed along the  $c$  axis in the LT range is a result of the simultaneous reduction of several bond lengths and angular distortions: i) decrease of Ow2–H3 $\cdots$ O2 hydrogen bonds oriented approximately along the  $c$  axis; ii) shrinkage of  $M3\text{O}_3(\text{H}_2\text{O})_3$  octahedra evidenced by the decrease in  $M3\text{--O}3$  and  $M3\text{--Ow}3$  bonds. The nature of the expansion of the coquimbite structure during the Stage II is better understood in terms of the orientation of  $[M2M3_2(\text{SO}_4)_6(\text{H}_2\text{O})_6]^{3-}$  clusters along the  $c$  axis.  $M\text{--O}$  and  $\text{S--O}$  bonds are only slightly affected by the temperature rise at Stage II, whereas O–H $\cdots$ O angular transformations seem to be the main driving force for the expansion of the coquimbite structure along the  $\alpha_{11}$  direction upon heating.

Coquimbite exhibits distinct magnetic properties compared to other iron sulfates, driven by antiferromagnetic interactions within its  $M3\text{--}M2\text{--}M3$  trimeric clusters of  $\text{Fe}^{3+}$ . The presence of  $\text{Al}^{3+}\text{--}\text{Fe}^{3+}$  site mixing in coquimbite introduces structural disorder, partially disrupting its magnetic ordering and contributing to magnetic entropy and magnetization features, such as a 1/3 magnetization plateau.

**Keywords:** coquimbite; sulfates; iron; non-ambient single crystal X-ray diffraction, magnetism, non-ambient powder X-ray diffraction, thermal expansion, thermal analysis, Mars

## 1. Introduction

Hydrated sulfate minerals with transition metals receive considerable attention from the viewpoint of environmental science (Brown Jr. and Calas 2011), as they are involved in various natural processes, including critical ecological impacts. Hydrated iron sulfates are also observed in extraterrestrial conditions, in particular, on the surface of Mars (Bibring and Langevin 2008 and references therein). Under Mars surface conditions, a wide range of Fe<sup>3+</sup> efflorescent sulfates has been determined (King and McSween 2005; King et al. 2008; Wang and Ling 2011), with most of them being oxidation products of sulfides (predominantly pyrrhotite). The significance of examining the transformations of sulfate minerals occurring on the surface of Mars has been recognized in the context of the potential implementation of the Mars Sample Return Mission (Tosca et al. 2022). A particular emphasis has been placed on the necessity of obtaining data on sulfate transformations across a broad temperature range (MEPAG, 2008), as well as on dehydration processes and their stability under fixed relative-humidity conditions (Tosca et al. 2022). The majority of the studies on the dehydration (Liu and Wang 2015) and on the phase transitions of iron sulfates (Wang et al. 2012, Apopei et al. 2014, Buzatu et al. 2016) have utilized Raman and NIR techniques. The utilization of X-ray diffraction techniques for further exploration of this matter will provide novel insights into the intricate transformations of natural iron sulfates in diverse environments.

Despite their structural diversity and presence in various geological and extraterrestrial environments, the study of magnetic properties of iron sulfate minerals remains limited compared to iron sulfides (Carrero et al. 2023). One of the most studied iron sulfates is jarosite  $\text{KFe}_3(\text{SO}_4)_2(\text{OH})_6$ , which has been the focus of extensive research due to its intriguing magnetic behavior arising from the frustrated antiferromagnetism of its kagome lattice of Fe<sup>3+</sup> ions. This unique lattice arrangement prevents complete magnetic ordering, making jarosite a model system for studying spin frustration (Klein et al. 2018). Jarosite has also garnered interest in planetary science, particularly for understanding Martian surface mineralogy and magnetic anomalies (Mills

et al. 2013). The magnetic properties of most other iron sulfate minerals remain largely unexplored. For iron sulfate minerals containing both  $\text{Fe}^{2+}$  and  $\text{Fe}^{3+}$  ions, magnetic studies have primarily focused on voltaite  $\text{K}_2\text{Fe}_5^{2+}\text{Fe}_3^{3+}\text{Al}(\text{SO}_4)_{12}\cdot 18\text{H}_2\text{O}$ , a complex hydrated sulfate with mixed valence states (Hermon et al. 1976). Voltaite's magnetic behavior reflects its intricate structural framework, which allows for various exchange interactions between Fe ions, though detailed mechanisms remain underexplored. Recent advancements include the discovery and magnetic characterization of a synthetic mikasaite structurally-related guanidinium-templated hydrous iron sulfate,  $(\text{CN}_3\text{H}_6)[\text{Fe}^{2+}\text{Fe}^{3+}(\text{SO}_4)_3(\text{H}_2\text{O})_3]$ . This material features a mixed  $S = 2$  and  $S = 5/2$  honeycomb spin lattice, derived from the rhombohedral structure of mikasaite  $\text{Fe}_2(\text{SO}_4)_3$ . The honeycomb spin arrangement introduces novel magnetic interactions and ordering phenomena, expanding the understanding of how structural topology influences magnetic behavior in iron sulfates (Ginga et al. 2023).

The crystal structure of coquimbite has been determined almost half a century ago (Fang and Robinson 1970; Giacobozzo et al. 1970), and has been further studied in detail (Majzlan et al. 2006, 2010; Demartin et al. 2010; Yang and Giester 2018). Special attention was given to the octahedral site occupancies and speciation role of  $\text{Fe}^{3+}$  and  $\text{Al}^{3+}$ . In a recent publication by Mauro et al. (2020), a comprehensive review of all published data on coquimbite is given. Based on the original structural data, a significant revision of the role of  $\text{Fe}^{3+}/\text{Al}^{3+}$  occupancies was conducted, resulting in the re-definition of the mineral formula.

We present herein a comprehensive study of the thermal and magnetic behavior of coquimbite over a wide temperature range.

## **2. Materials and methods**

### ***2.1 Mineral occurrence***

The studied sample containing coquimbite (Fig. 1) was collected by one of the authors (OIS) in January 2016 at the Alcaparrosa mine, El Loa Province, Antofagasta, Chile (for more

details regarding the mine see Bandy (1938)) and formed in highly arid climate. In the collected samples, coquimbite is represented by large purple transparent crystals in close association with dark red-brown aggregates of römerite. Coquimbite crystals are enclosed by aluminocopiapite. Due to the relatively large amount of water molecules per formula unit in coquimbite, only a qualitative microprobe analysis was possible (TM 3000 HITACHI) which revealed no elements with an atomic number greater than 11 (Na) other than Al, Fe and S. For all studies, individual crystals of coquimbite were carefully separated from the bulk sample.

## ***2.2 Low temperature and high temperature single-crystal X-ray diffraction (LT-SCXRD and HT-SCXRD)***

The temperature-dependent single crystal X-ray diffraction data for coquimbite at temperatures from  $-173\text{ }^{\circ}\text{C}$  to  $77\text{ }^{\circ}\text{C}$  were obtained using a Rigaku XtaLAB Synergy-S diffractometer equipped with a micro-focus sealed X-ray tube (MoK $\alpha$  radiation; operating at 50 kV and 1.0 mA), HyPix-6000HE detector and Oxford Cryostream 800 (Oxford, UK) cooling system. The single crystal was mounted on the quartz glass fiber, which was placed into the quartz capillary. A complete data set was collected in the mentioned temperature range with  $10\text{ }^{\circ}\text{C}$  steps. An empirical absorption correction based on the spherical harmonics implemented in the SCALE3 ABSPACK algorithm was applied in the CrysAlisPro v171.41.64.86a program (Agilent 2014). Selected unit-cell parameters in  $P\bar{3}c$  space group and refinement parameters are given in Table 1. All H atoms were located from the analysis of difference-Fourier electron density maps. O–H distances were left unconstrained. The structural data were refined only up to  $77\text{ }^{\circ}\text{C}$  (350 K), since the  $R_{\text{int}}$  value is above 10 % at higher temperatures. Note, the SCXRD frames have reflections up to  $130\text{ }^{\circ}\text{C}$  with unit-cell metrics corresponding to coquimbite.

The thermal motions of atoms have an effect on the bond lengths obtained during the single-crystal X-ray diffraction (Downs 2000). Corrections for bonds lengths in HT-SCXRD in coquimbite were calculated using a formula for the rigid-body motion:

$$R_{SRB}^2 = R_{obs}^2 + \frac{3}{8\pi^2} (B_{eq}(Y) - B_{eq}(X))$$

where  $R_{SRB}$  and  $R_{obs}$  are corrected and observed Y–X bond lengths, respectively;  $B_{eq}(X)$  and  $B_{eq}(Y)$  are equivalent temperature factors of X (central atom) and Y (ligand), respectively. The thermal parameters  $U_{ij}$  instead of  $B_{ij}$  were used and implemented in the CIF-files, taking into account the IUCr recommendations (Trueblood et al. 1996). Due to above-mentioned corrections, bond length values are given in the text below without e.s.d. Typical e.s.d. for the uncorrected Fe–O and S–O bond-length values are of 0.001–0.002 Å.

### **2.3 Low temperature and high temperature powder X-ray diffraction (LT-PXRD and HT-PXRD)**

For the variable-temperature XRD experiments, diffraction patterns were registered on a Rigaku Ultima IV powder diffractometer (Rigaku R-300 camera, low vacuum of 600 Pa, CoK $\alpha$  radiation for the temperature range –180 °C to 200 °C and Rigaku HTA-1600 camera and low vacuum of 600 Pa, CoK $\alpha$  radiation for the 25 °C to 740 °C range, linear PSD detector). The ground sample was suspended in dry heptane and transferred onto a Pt–Rh holder. The heating rate was 2 °C/min. Phase analysis was performed based on the PDF–2 database (powder diffraction file from the International Centre for Diffraction Data, <http://www.icdd.com/>, accessed 2020), and PDXL (Rigaku 2014) and TOPAS V.5.0 (Bruker-AXS 2014) software. Thermal expansion of coquimbite was calculated using the *RietveldToTensor* program (Bubnova et al. 2018).

Before raising the temperature, it was verified that coquimbite did not lose water or decompose when the Rigaku R-300 camera was evacuated. Identical PXRD patterns were obtained at room temperature with and without the vacuum camera.

The results of variable-temperature powder X-ray diffraction are shown in Figure 2. Coquimbite is stable up to 145 °C. Between 150 °C to 225 °C, the sample becomes amorphous. The recrystallization product is a mikasaite-like phase (Fe,Al)<sub>2</sub>(SO<sub>4</sub>)<sub>3</sub> (Miura et al. 1994)

which is stable up to 575 °C. According to the structure refinement of mikasaite, the ratio of iron and aluminum in anhydrous sulfate is identical to that in primary coquimbite. This indicates that there are no additional amorphous phases in which part of the aluminum and iron may undergo crystallization.

#### **2.4 Thermal analysis**

Thermal behavior of coquimbite (Figure 3) was investigated on a NETZSCH STA 429 CD thermoanalyzer using TG+DSC sample holders and Pt/Pt-Rh thermocouples (S type). The initial sample weight was 7.0 mg. The measurements were carried out at a heating rate of 10 °C/ min in the temperature range from 25 to 800 °C. The TG (%) and DSC (mW/mg) data were recorded simultaneously.

The TG curve shows three stages of mass loss (Figure 3). The TG curve is almost straight when heated in the range of from 72 to 121 °C. The DSC curve exhibits a significant endothermic effect in the temperature range of from 121 to 210 °C, with a peak at 164 °C. This corresponds to the initial stage of loss in the TG curve, which is 15.97 wt %. Stage I corresponds to the first stage of the dehydration and removal of weakly bound water in a cyclohexane-like arrangement (see below). Three endothermic peaks of varying intensity are observed in stage II between 210 and 321 °C, representing a loss of 9.52 wt %. From the powder X-ray diffraction data, it appears that the remaining water is most likely removed from the amorphous phase/phases at this stage. The absence of a discernible peak indicating the crystallization of mikasaite suggests that this process is sluggish. At stage III, within the temperature range of 584 to 775 °C, a significant endothermic effect is observed on the DSC curve, with a peak at 752 °C, corresponding to a loss of 37.53 wt. %. This stage marks the desulfurization of mikasaite  $\text{Fe}_2(\text{SO}_4)_3$ , which then transforms into hematite  $\text{Fe}_2\text{O}_3$ .

#### **2.5 Magnetic Measurements**

Magnetic susceptibility ( $\chi$ ) as a function of temperature was analyzed on a 22.8 mg polycrystalline sample of coquimbite. The measurements were taken at fields of 0.01 T, 0.1 T, 1 T, and 5 T over a temperature range of 2 to 280 K. The measurements were performed using a Quantum Design MPMS-XL magnetometer in magnetic fields reaching up to 7 T. For the temperature-dependent magnetization measurements, both zero-field-cooling (ZFC) and field-cooling (FC) protocols were utilized. Sample chamber was flushed with helium gas and evacuated to about  $10^{-2}$  atm prior to the measurements.

The Heat capacity ( $C_p$ ) measurements were performed on a pressed pellet with the total mass of 10.5 mg in the temperature range of 1.8 K to 200 K in zero field and under external magnetic field of 9 T using the dedicated option of the Physical Property Measurements System (PPMS) from Quantum Design.

Thermodynamic properties were obtained from classical Monte Carlo simulations on spin-5/2 trimer-based cluster. The simulations were performed using the ALPS simulation package (Albuquerque et al. 2007).

### 3. Results

#### 3.1 Crystal structure

The crystal structure of coquimbite (Figure 4a,b) is composed of isolated  $[M1(H_2O)_6]^{3+}$  octahedra and  $[M2M3_2(SO_4)_6(H_2O)_6]^{3-}$  clusters, where  $M$  cations ( $M = Al$  and  $Fe$ ) center  $M1(H_2O)_6$ ,  $M2O_6$ , and  $M3O_3(H_2O)_3$  octahedra. The  $M2O_6$  octahedron shares all of its vertices with sulfate tetrahedra, resulting in a fragment of the anhydrous  $Fe_2(SO_4)_3$  mikasaite structure. The  $M3$ -centered octahedron has only three common vertices with sulfate tetrahedra, and the remaining three are occupied by oxygen atoms of water molecules. The  $Al^{3+}$  predominantly occupies the  $M1$  position ( $2b$  site),  $Al_{0.930(6)}Fe_{0.071(6)}$ . Observed  $M3$ -site occupancy is similar to that one observed in coquimbite from Monte Arsiccio mine, Apuan Alps, Tuscany, Italy (Mauro et al. 2020) and in coquimbite from

Richmond mine at Iron Mountain, near Redding, California (Majzlan et al. 2006). In general, it agrees well to the previously reported data for coquimbite crystals from different localities (Table 2). The Fe-dominant positions *M2* (*2c* site) and *M3* (*4f* site) contain very little aluminum: Fe<sub>0.956(7)</sub>Al<sub>0.044(7)</sub> and Fe<sub>0.960(5)</sub>Al<sub>0.040(5)</sub>, respectively. The average  $\langle M-O \rangle$  bond lengths in *M1*(H<sub>2</sub>O)<sub>6</sub>, *M2*O<sub>6</sub>, and *M3*O<sub>3</sub>(H<sub>2</sub>O)<sub>3</sub> octahedra are 1.890 Å, 1.999 Å, and 1.991 Å, respectively, which almost coincides with the statistical data for  $\langle Al-O \rangle = 1.903$  Å (Gagné and Hawthorne 2018) and  $\langle Fe^{3+}-O \rangle = 2.015$  Å (Gagné and Hawthorne 2020). Bond-valence sums for *M1*, *M2* and *M3* sites are 3.12 *v.u.*, 3.12 *v.u.*, and 3.21 *v.u.*, respectively. One symmetry independent S1 atom (*12i* site) has an average bond length of 1.478 Å (5.92 *v.u.*), which is consistent with Yang and Giester (2018) and Mauro et al. (2020).

Three symmetrically independent water molecules form a complex hydrogen bonding system in the coquimbite structure. The H $\cdots$ A and D-H $\cdots$ A angle values are given below for the SCXRD dataset collected at -173 °C (100 K). The Ow1 molecule (H1 and H2 atoms) is located in the vertices of the [*M1*(H<sub>2</sub>O)<sub>6</sub>]<sup>3+</sup> octahedra and forms hydrogen bonds to the O2 and O1 oxygen atoms of the terminal vertices of the sulfate tetrahedra with H $\cdots$ A distances of 1.93(3), 1.79(3) Å and D-H $\cdots$ A angles of 172(3)° and 170(3)°. The free Ow2 molecules (H3, H4a, and H4b atoms) produce an arrangement described either as a cyclohexane-like chair (Demartin et al. 2010) or as a polyhedron centered by a vacancy (Majzlan et al. 2010). Half-occupied positions H4a and H4b are linked via hydrogen bonds to neighboring molecules of the Ow2 ring with H $\cdots$ A distances of 1.86(4), 2.02(5) Å and D-H $\cdots$ A angles of 162(4)° and 162(5)°. The cyclohexane-like chair is linked to neighboring [*Fe*<sub>3</sub>(SO<sub>4</sub>)<sub>6</sub>(H<sub>2</sub>O)<sub>6</sub>]<sup>3-</sup> clusters via hydrogen bonds H3 $\cdots$ O2 with an H $\cdots$ A distance of 1.96(3) Å and a D-H $\cdots$ A angle of 158(3)°. [*Fe*<sub>3</sub>(SO<sub>4</sub>)<sub>6</sub>(H<sub>2</sub>O)<sub>6</sub>]<sup>3-</sup> clusters are terminated by Ow3 molecules (H5 and H6 atoms). The acceptor for the H5 is the sulfate oxygen O1 with H $\cdots$ A = 1.89(3) Å and D-H $\cdots$ A = 167(3)°. The H6 atom is bonded to the Ow2 atom with H $\cdots$ A at 1.85(3) Å and D-H $\cdots$ A at 175(3)°.

### 3.2 Crystal structure evolution upon heating

The temperature dependencies of the unit-cell parameters and volume of coquimbite are shown in Figure 5. From the graphs, it appears that the behavior of coquimbite with increasing temperature can be divided into two stages. At stage I, in the range from  $-173$  to  $-143$  °C, the  $a$  parameter decreases from  $10.8904(3)$  to  $10.8823(3)$  Å, whereas the  $c$  parameter increases from  $17.0731(4)$  to  $17.0899(6)$  Å. The unit-cell volume decreases from  $1753.61(10)$  to  $1752.70(12)$  Å<sup>3</sup>.

The temperature dependence of the unit-cell parameters of coquimbite at stage I can be described by the following equations:

$$a_t = 10.846(16) - 0.265(103) \times 10^{-5}T$$

$$c_t = 17.160(26) + 0.516(167) \times 10^{-5}T$$

$$V_t = 1748(3) - 0.0033(19) \times 10^{-5}T, \text{ where } T \text{ is a temperature in } ^\circ\text{C}.$$

Further, starting from  $-133$  °C (stage II), the unit-cell expands along all crystallographic axes from  $a = 10.8856(3)$ ,  $b = 17.0738(5)$  Å,  $V = 1752.12(10)$  Å<sup>3</sup> to  $a = 10.9387(3)$ ,  $b = 17.0817(5)$  Å,  $V = 1770.08(11)$  Å<sup>3</sup>:

$$a_t = 10.9166(8) + 0.225(11) \times 10^{-3}T$$

$$c_t = 17.0823(15) + 0.026(21) \times 10^{-3}T$$

$$V_t = 1763.0(3) + 0.0075(4) \times 10^{-1}T, \text{ where } T \text{ is a temperature in } ^\circ\text{C}.$$

The thermal expansion of coquimbite exhibits a significant anisotropy in both stages (Figure 4c). Nevertheless, the direction of thermal expansion of the structure exhibits a significant divergence. In the range of  $-173$  to  $-143$  °C, the  $\alpha_{33}$  direction exhibits positive thermal expansion, whereas the  $\alpha_{11}$  direction exhibits a strong negative expansion. The thermal expansion of coquimbite in the range of  $-133$  to  $77$  °C is solely positive. The structure exhibits a predominant expansion along the  $a$  axis, whereas it exhibits virtually no variation along the  $c$  axis, as depicted in Figure 5.

The temperature-dependent variation in bond lengths (Table 3, Figure 6) has been observed in the *M*-centered octahedra and sulfate tetrahedra in the structure of coquimbite. The *M*1–Ow1 bonds in the isolated *M*1(H<sub>2</sub>O)<sub>6</sub> octahedra change only slightly upon heating, and they increase from 1.895 Å at 100 K to 1.900 Å at 350 K ( $\Delta_d = 0.005$  Å). The *M*2–O4 bond in the *M*2O<sub>6</sub> octahedron shows an increase by  $\Delta_d = 0.009$  Å (2.001 Å at 100 K and 2.010 at 350 K). In the *M*3O<sub>3</sub>(H<sub>2</sub>O)<sub>3</sub> octahedra, the *M*3–O3 bonds bridging to the SO<sub>4</sub> tetrahedra, show a decrease from 1.983 Å at 100 K to 1.978 Å at 350 K, i.e.  $\Delta_d = -0.005$  Å. In contrast, the *M*3–Ow3 bond increases from 2.005 at 100 K to 2.016 at 350 K ( $\Delta_d = 0.011$  Å) with a rebound down to 2.003 Å at 150 K. The S1–O1<sub>t</sub> (t = terminal oxygen in SO<sub>4</sub> tetrahedron) bond length remains virtually intact over studied temperature range. The S1–O2<sub>t</sub> bond decreases slightly from 1.465 Å at 100 K to 1.463 Å at 350 K ( $\Delta_d = -0.002$  Å). The S1–O3<sub>br</sub> (br = bridging oxygen) bond increases upon heating from 1.492 Å to 1.496 Å ( $\Delta_d = 0.004$  Å). And the S1–O4<sub>br</sub> bond decreases from 1.493 Å to 1.489 Å ( $\Delta_d = -0.004$  Å).

Significant O–H···O angular distortions (Figure 7) are observed in the crystal structure of coquimbite upon heating (Table 3). The following angles are particularly prone to bending: (i) Ow1–H2···O1, i.e. between an isolated *M*1(H<sub>2</sub>O)<sub>6</sub> octahedron and *M*2*M*3<sub>2</sub>(SO<sub>4</sub>)<sub>6</sub>(H<sub>2</sub>O)<sub>6</sub> cluster; (ii) Ow2–H3···O2, i.e. between a cyclohexane ring and *M*2*M*3<sub>2</sub>(SO<sub>4</sub>)<sub>6</sub>(H<sub>2</sub>O)<sub>6</sub> cluster; (iii) Ow3–H5···O1, i.e. between two adjacent *M*2*M*3<sub>2</sub>(SO<sub>4</sub>)<sub>6</sub>(H<sub>2</sub>O)<sub>6</sub> clusters. Ow1–H2···O1 decreases from 170(3)° at 100 K to 162(3)° at 350 K ( $\Delta_{\text{ang}} = 8^\circ$ ). Also, a decrease in the angle is observed for the Ow2–H3···O2 bond from 158(3)° to 148(3)° ( $\Delta_{\text{ang}} = 10^\circ$ ) with a sharp decrease after 300 K. An increase in the angle is observed for the Ow3–H5···O1 from 167(3)° to 176(3)° ( $\Delta_{\text{ang}} = 9^\circ$ ). The changes in the **D**···**A** distances are in the range 0.005 (Ow3–H6···Ow2) - 0.018 (Ow2–H4a···Ow2).

### 3.3 Magnetic properties

From the point of view of magnetism,  $M3-M2-M3$  trimers can be distinguished in the crystal structure of coquimbite (Figure 4a, Figure 7). The nearest-neighbor Fe–Fe distances in the coquimbite structure involve  $SO_4$  tetrahedra. The  $M3-M2$  and  $M3-M3$  distances are 4.3 Å and 6.3 Å, respectively. The temperature dependence of the molar magnetic susceptibility for coquimbite measured in the applied fields of 0.01 T, 0.1 T, 1 T and 5 T is shown in Figure 8a. The Curie–Weiss fit with  $\chi = C/(T - \theta)$  above 100 K returns  $C = 12.5$  emu K/mol, and  $\theta = -7.7$  K. The value of the Curie constant  $C = ng^2S(S + 1)\mu_B^2N_A/3k_B$ , where  $\mu_B$ ,  $N_A$ , and  $k_B$  are Bohr, Avogadro, and Boltzmann constants, respectively, is consistent with the  $g$ -factor  $g \approx 2$  for  $n = 3$   $Fe^{3+}$  ions per formula unit in the  $S = 5/2$  high-spin state. This corresponds to the effective moment of  $\mu = 10 \mu_B/f.u.$ , which is in a good agreement with  $10.2 \mu_B/f.u.$  expected for three spin-5/2  $Fe^{3+}$  ions.

Field-dependent magnetization shows a rapid increase in the applied field. No saturation could be observed in the MPMS measurement up to 7 T. Moreover, the magnetization rapidly reaches the 1/3 plateau value of  $M_s/3 \sim 5.1 \mu_B$  which persists to  $B_c \sim 6$  T. On the other hand, our simulated magnetization curve based on with intratrimer interaction  $J = 2.4$  K indicates the saturation  $M_s \sim 15.4 \mu_B/f.u.$  that is reached at  $B_s \sim 18$  T (Figure 8b). This modified fit of  $\chi(T)$  dependence at 0.01 T based on described spin  $S = 5/2$  trimer model is shown in Figure 8a, inset.

The negative value of the  $T_\theta$  temperature indicates that dominant exchange interactions are antiferromagnetic. The Fe–Fe–Fe trimers elongated along the  $c$  axis can be distinguished in the crystal structure of the coquimbite. With the distances of 4.3 Å and corresponding strongest intratrimer interaction  $J = 2.4$  K, these trimers together with a long and weaker intertrimer-interactions elucidate the negative Curie-Weiss temperature.

Temperature-dependent heat capacity of coquimbite is dominated by the lattice contribution and does not reveal any anomalies between 1.8 and 200 K (Figure 9a). Heat capacity increases with temperature due to the dominant phonon contribution. The low-temperature behaviour of the heat capacity below 15 K further reveals by the field dependence a small magnetic

contribution. At room temperature, the specific heat  $C_p$  is far from the thermodynamic limit  $3Rn = 2195 \text{ J/mol K}$ .

To estimate the magnetic entropy associated with these  $\text{Fe}^{3+}$  ions, we determined the phonon contribution  $C_p^{ph}$  to the heat capacity  $C_p$  by fitting the data above 10 K with a sum of three Debye functions and the  $A/T^2$  term that corresponds to the high-temperature limit of the magnetic contribution:

$$C_p(T) = \frac{A}{T^2} + \sum_{i=1}^3 g_i C_{Deb,i}(\theta_{Deb,i}, T),$$

where  $A$  is the fitting constant. The sum of the different  $g_i$  ( $g_1 = 5$ ,  $g_2 = 18$ ,  $g_3 = 29$ ) is equal to the total number of atoms with the exception of light hydrogens in the formula unit of coquimbite (in total: 88 atoms, without hydrogen: 52 atoms). The Debye functions are given by:

$$C_{Deb,i}(\theta_{Deb,i}, T) = 9R \left(\frac{T}{\theta_{Deb,i}}\right)^3 \int_0^{\theta_{Deb,i}/T} \frac{x^4 e^x}{(e^x - 1)^2} dx,$$

where  $R$  is the gas constant and  $\theta_{Deb,i}$  are the corresponding Debye temperatures ( $\theta_{Deb,1} = 108 \text{ K}$ ,  $\theta_{Deb,2} = 1224 \text{ K}$ ,  $\theta_{Deb,3} = 446 \text{ K}$ ). In this analysis, we basically neglect the contribution from the Fe trimers because it is expected to be very small compared to the lattice contribution.

Magnetic heat capacity associated with the  $\text{Fe}^{3+}$  ions is obtained by subtracting the phonon contribution from the experimental heat capacity (Figure 9b). The resulting magnetic entropy of coquimbite at 9 T is about 55% of the total entropy of  $S_{mag} = R \cdot (3 \ln 6) = 44.69 \text{ J/mol} \cdot \text{K}$  due to the 3  $\text{Fe}^{3+}$  ions and corroborates our assignment of the saturated magnetization to the response of the paramagnetic substitutions in the  $M2$  and  $M3$  sites.

## Discussion

The structural feature of coquimbite from Alcaparrosa demonstrates a strong preference of  $\text{Al}^{3+}$  to the sites coordinated only by water molecules. Being a strong Lewis acid,  $\text{Al}^{3+}$  forms relatively strong bonds to the coordinating water molecules, and at ambient temperatures, its coordination sphere can be considered relatively inert. On the contrary, the coordination sphere of  $\text{Fe}^{3+}$  (high spin  $3d^5$ , CFSE = 0) exchanges ligands more easily; therefore, direct coordination of

$\text{Fe}^{3+}$  to the sulfate anion is not surprising. Upon synthesis of other Al/Fe sulfates, e.g. voltaite analogs,  $\text{Al}^{3+}$  retains its hydration shell even under high concentrations of sulfuric acid; the presence of  $[\text{Al}(\text{H}_2\text{O})_6]^{3+}$  cations is claimed to be a necessary condition for the formation of voltaite structure.

As mentioned earlier, a limited number of studies have been published regarding the thermal expansion of hydrated sulfate minerals, primarily pertaining to the most prevalent ones. The structural transformations of calcium sulfate, gypsum  $\text{Ca}(\text{SO}_4)\cdot 2\text{H}_2\text{O}$ , bassanite  $\text{Ca}(\text{SO}_4)\cdot 0.5\text{H}_2\text{O}$  and anhydrite  $\text{Ca}(\text{SO}_4)$  were studied (Ballirano and Melis 2009a,b,c; Kyono et al. 2022). The phenomenon of negative thermal expansion in hydrated sulfates has been elucidated in magnesium sulfates, including epsomite  $\text{Mg}(\text{SO}_4)\cdot 7\text{H}_2\text{O}$  (Fortes et al. 2006) and meridianite  $\text{Mg}(\text{SO}_4)\cdot 11\text{H}_2\text{O}$  (Fortes et al. 2008), as well as kieserite-type compounds  $M(\text{SO}_4)(\text{H}_2\text{O})$  ( $M = \text{Mg}, \text{Fe}, \text{Co}, \text{Ni}$ ) (Wildner et al. 2022). In the latter case, negative thermal expansion was observed to be associated with cooperative polyhedral rotation, a characteristic feature of chain structural motifs.

In coquimbite, all the  $\text{O}-\text{H}\cdots\text{O}$  bonds remain virtually intact during Stage 1 except for  $\text{Ow}2-\text{H}3\cdots\text{O}2$  (Table 3). The negative thermal expansion observed along the  $c$  axis in the low-temperature range is a result of the simultaneous reduction of several bond lengths and angular distortions: i) decrease of  $\text{Ow}2-\text{H}3\cdots\text{O}2$  hydrogen bonds (Table 3) oriented approximately along the  $c$  axis; ii) shrinkage of  $M3\text{O}_3(\text{H}_2\text{O})_3$  octahedra evidenced by the decrease of  $M3-\text{O}3$  and  $M3-\text{Ow}3$  bonds (Figure 6c).

The nature of the expansion of the coquimbite structure during the Stage II is better understood in terms of the orientation of  $[\text{M}2\text{M}3_2(\text{SO}_4)_6(\text{H}_2\text{O})_6]^{3-}$  clusters (Figure 4a) along the  $c$  axis.  $M-\text{O}$  and  $\text{S}-\text{O}$  bonds are only slightly affected to the temperature rise in Stage II, whereas  $\text{O}-\text{H}\cdots\text{O}$  angular transformations of the several hydrogen bonds (Figure 7) seem to be the main driving force for the expansion of the coquimbite structure along the  $\alpha_{11}$  direction upon heating.

Coquimbite exhibits distinct magnetic properties compared to other iron sulfates, driven by antiferromagnetic interactions within its  $M3-M2-M3$  trimeric clusters of  $Fe^{3+}$ . This contrasts with the spin frustration observed in jarosite  $KFe_3(SO_4)_2(OH)_6$ , where a kagome lattice of  $Fe^{3+}$  ions prevents full magnetic ordering, resulting in a complex frustrated antiferromagnetic state (Klein et al. 2018). In comparison to voltaite  $K_2Fe_5^{2+}Fe_3^{3+}Al(SO_4)_{12} \cdot 18H_2O$ , coquimbite lacks the intricate  $Fe^{2+}-Fe^{3+}$  interactions but compensates with high-spin  $Fe^{3+}$  ions that dominate its magnetic behavior. The presence of  $Al^{3+}-Fe^{3+}$  site mixing in coquimbite introduces structural disorder, partially disrupting its magnetic ordering and contributing to magnetic entropy and magnetization features, such as a  $1/3$  magnetization plateau. Furthermore, while synthetic guanidinium-templated hydrous iron sulfate  $(CN_3H_6)[Fe^{2+}Fe^{3+}(SO_4)_3(H_2O)_3]$  displays a honeycomb spin lattice derived from mikasaite (Ginga et al. 2023), coquimbite's  $M3-M2-M3$  trimeric exchange mechanism represents a new avenue for the study of antiferromagnetic systems in hydrated sulfate minerals. Its magnetic properties not only highlight the diversity of behaviors within iron sulfates but also underscore the structural influences on spin interactions and magnetic entropy in these minerals.

## Implications

Previously, the thermal behavior of several hydrated sulfates, particularly coquimbite, was studied using Raman spectroscopy (Apopei et al. 2014) and NIR spectroscopy (Buzatu et al. 2016) under stepwise heating conditions and recording spectra after cooling to a room temperature. A transition from coquimbite to mikasaite was reported at  $50\text{ }^\circ\text{C}$ , followed by amorphisation at  $150\text{ }^\circ\text{C}$  (Buzatu et al. 2016). Our investigations by both single crystal and powder LT/HT *in situ* X-ray diffraction have revealed evidence indicating a broader temperature range for the mineral's stability, with a gradual transition of coquimbite  $AlFe_3(SO_4)_6(H_2O)_{12} \cdot 6H_2O$  to the amorphous phase at  $150\text{ }^\circ\text{C}$ . Subsequently, a transition to a mikasaite-like phase  $(Fe,Al)_2(SO_4)_3$  occurred at

250 °C, followed by a second amorphization at 600 °C, ultimately leading to the crystallization of hematite.

Previously the determination of various sulfates on the surface of Mars has raised concerns regarding their stability under freezing and vacuum conditions, which may be feasible during sample delivery to Earth (Tosca et al., 2022). Particular attention was given to the ease of dehydration of sulfates, accompanied by mineral transformations. The average surface pressure on Mars is ~ 600 Pa (i.e., a low vacuum). The average surface temperature is -63 °C (210 K) and may reach ~ 20 °C (293 K) during the daytime on the equator. The lowest temperature measured *in situ* is about -153 °C (120 K) at the poles. We observed that coquimbite is stable at temperatures between -180 °C and 145 °C and a low vacuum of 600 Pa. These environments are similar to those observed on Mars, but they are not identical (i.e. in terms of CO<sub>2</sub> content). Our research shows that coquimbite is much more stable over a wide Mars-like temperature range, compared, e.g., to römerite and copiapite group minerals often associated with it. The presence of coquimbite and other iron sulfates in these environments may serve as an indicator of pH,  $p(\text{O}_2)$ , and component activity (Fe, O<sub>2</sub>, SO<sub>4</sub>, H<sub>2</sub>O) on Mars in the past (King and McSween 2005).

## Acknowledgements

We thank two anonymous reviewers for their comments, which improved the manuscript. Technical support (project # 118201839) by the SPbSU X-ray Diffraction Resource Center is gratefully acknowledged. V.A.G. thanks Alexander A. Tsirlin for stimulating discussions, and his support provided in analyzing the magnetic properties. V.A.G. was financially supported by DAAD (grant # 91837667).

## References

1. Agilent. (2014) CrysAlisPro. Agilent Technologies Ltd, Yarnton, Oxfordshire, England.
2. Albuquerque, A., Alet, F., Corboz, P., Dayal, P., Feiguin, A., Fuchs, S., Gamper, L., Gull, E., Gürtler, S., Honecker, A., and others. (2007). The ALPS project release 1.3: Open-source

software for strongly correlated systems. *Journal of Magnetism and Magnetic Materials*, 310, 1187–1193.

3. Apopei, A.I., Buzgar, N., Damian, G., and Buzatu, A. (2014) The Raman study of weathering minerals from the Coranda-Hondol open pit (Certej gold-silver deposit) and their photochemical degradation products under laser irradiation. *The Canadian Mineralogist*, 52, 1027–1038.
4. Ballirano, P., and Melis, E. (2009a) Thermal behaviour and kinetics of dehydration of gypsum in air from in situ real-time laboratory parallel-beam X-ray powder diffraction. *Physics and Chemistry of Minerals*, 36, 391–402.
5. Ballirano, P., and Melis, E. (2009b) Thermal behaviour and kinetics of dehydration in air of bassanite, calcium sulphate hemihydrate ( $\text{CaSO}_4 \cdot 0.5\text{H}_2\text{O}$ ), from X-ray powder diffraction. *European Journal of Mineralogy*, 21, 985–993.
6. Ballirano, P., and Melis, E. (2009c) The thermal behaviour of  $\gamma\text{-CaSO}_4$ . *Physics and Chemistry of Minerals*, 36, 319–327.
7. Bandy, M.C. (1938) Mineralogy of three sulfate deposits of northern Chile. *American Mineralogist*, 23, 669–760.
8. Bibring, J., and Langevin, Y. (2008) Mineralogy of the Martian surface from Mars Express OMEGA observations. In J. Bell, Ed., *The Martian Surface: Composition, Mineralogy and Physical Properties*, p. 151–168. Cambridge University Press, UK.
9. Brown, G.E. Jr., and Calas, G. (2011) Environmental mineralogy – Understanding element behavior in ecosystems. *Comptes Rendus Geoscience*, 343, 90–112.
10. Bubnova, R.S., Firsova, V.A., Volkov, S.N., and Filatov, S.K. (2018) RietveldToTensor: program for processing powder X-ray diffraction data under variable conditions. *Glass Physics and Chemistry*, 44, 33–40.

11. Buzatu, A., Dill, H.G., Buzgar, N., Damian, G., Maftei, A.E., and Apopei, A.I. (2016) Efflorescent sulfates from Baia Sprie mining area (Romania) — acid mine drainage and climatological approach. *Science of the Total Environment*, 542, 629–641.
12. Carrero, S., Slotznick, S.P., Fakra, S.C., Sitar, M.C., Bone, S.E., Mauk, J.L., Manning, A.H., Swanson-Hysell, N.L., Williams, K.H., Banfield, J.F., and Gilbert, B. (2023) Mineralogical, magnetic and geochemical data constrain the pathways and extent of weathering of mineralized sedimentary rocks. *Geochimica et Cosmochimica Acta*, 343, 180–195.
13. Demartin, F., Castellano, C., Gramaccioli, C.M., and Campostrini, I. (2010) Aluminum-for-iron substitution, hydrogen bonding, and a novel structure-type in coquimbite-like minerals. *Canadian Mineralogist*, 48, 323–333.
14. Downs, R.T. (2000) Analysis of harmonic displacement factors. In R.M. Hazen and R.T. Downs, Eds., *High-Temperature and High-Pressure Crystal Chemistry*, 41, p. 61–88. *Reviews in Mineralogy and Geochemistry*, Mineralogical Society of America, Chantilly, Virginia.
15. Fang, J.H., and Robinson, P.D. (1970) Crystal structures and mineral chemistry of hydrated ferric sulfates. I. The crystal structure of coquimbite. *American Mineralogist*, 55, 1534–1540.
16. Fortes, A.D., Wood, I.G., Alfredsson, M., Vočadlo, L., and Knight, K.S. (2006) The thermoelastic properties of  $\text{MgSO}_4 \cdot 7\text{D}_2\text{O}$  (epsomite) from powder neutron diffraction and ab initio calculation. *European Journal of Mineralogy*, 18, 449–462.
17. Fortes, A.D., Wood, I.G., and Knight, K.S. (2008) The crystal structure and thermal expansion tensor of  $\text{MgSO}_4 \cdot 11\text{D}_2\text{O}$  (meridianiite) determined by neutron powder diffraction. *Physics and Chemistry of Minerals*, 35, 207–221.
18. Gagné, O.C., and Hawthorne, F.C. (2018) Bond-length distributions for ions bonded to oxygen: metalloids and post-transition metals. *Acta Crystallographica*, B74, 63–78.

19. Gagné, O.C., and Hawthorne, F.C. (2020) Bond-length distributions for ions bonded to oxygen: results for the transition metals and quantification of the factors underlying bond-length variation in inorganic solids. *IUCrJ*, 7, 581–629.
20. Giacobazzo, C., Menchetti, S., and Scordari, F. (1970) The crystal structure of coquimbite. *Atti della Accademia Nazionale dei Lincei, Rendiconti della Classe di Scienze Fisiche, Matematiche e Naturali*, 49, 129–140.
21. Ginga, V.A., Siidra, O.I., Tsirlin, A.A., Setzer, A., Charkin, D.O., Börner, M., Abdulina, V.R., Ivanov, S.A., Gorbachevskaya, D.A., and Zolotov, N.A. (2023)  $(\text{CN}_3\text{H}_6)[\text{Fe}^{\text{II}}\text{Fe}^{\text{III}}(\text{SO}_4)_3(\text{H}_2\text{O})_3]$ : A framework iron sulfate with a mixed  $S = 2$  and  $S = 5/2$  honeycomb lattice. *Inorganic Chemistry*, 62, 17625–17633.
22. Hermon, E., Haddad, R., Simkin, D., Brandão, D.E., and Muir, W.B. (1976) Magnetic properties and the distribution of iron ions in voltaites. *Canadian Journal of Physics*, 54, 1149–1156.
23. King, P.L., and McSween, H.Y. Jr. (2005) Effects of  $\text{H}_2\text{O}$ , pH, and oxidation state on the stability of Fe minerals on Mars. *Journal of Geophysical Research: Planets*, 110, E12S10
24. King, P.L., Lane, M.D., Hyde, B.C., Dyar, M.D., and Bishop, J.L. (2008) Fe-sulfates in Mars: Considerations for martian environmental conditions, Mars sample return and hazards. *Ground truth from Mars: Science Payoff from a Sample Return Mission*. LPI, Albuquerque, p. 46–47.
25. Klein, R.A., Walsh, J.P.S., Clarke, S.M., Guo, Y., Bi, W., Fabbris, G., Meng, Y., Haskel, D., Alp, E.E., Van Duyne, R.P., Jacobsen, S.D., and Freedman, D.E. (2018) Impact of pressure on magnetic order in jarosite. *Journal of the American Chemical Society*, 140, 12001–12009.
26. Kyono, A., Ikeda, R., Takagi, S., and Nishiyasu, W. (2022) Structural evolution of gypsum ( $\text{CaSO}_4 \cdot 2\text{H}_2\text{O}$ ) during thermal dehydration. *Journal of Mineralogical and Petrological Sciences*, 117, 015.

27. Liu, Y., and Wang, A. (2015) Dehydration of Na-jarosite, ferricopiapite, and rhomboclase at temperatures of 50 and 95°C: implications for Martian ferric sulfates. *Journal of Raman Spectroscopy*, 46, 493–500.
28. Majzlan, J., Navrotsky, A., McCleskey, R.B., and Alpers, C.N. (2006) Thermodynamic properties and crystal structure refinement of ferricopiapite, coquimbite, rhomboclase, and  $\text{Fe}_2(\text{SO}_4)_3(\text{H}_2\text{O})_5$ . *European Journal of Mineralogy*, 18, 175–186.
29. Majzlan, J., Đorđević, T., Kolitsch, U., and Schefer, J. (2010) Hydrogen bonding in coquimbite, nominally  $\text{Fe}_2(\text{SO}_4)_3 \cdot 9\text{H}_2\text{O}$ , and the relationship between coquimbite and paracoquimbite. *Mineralogy and Petrology*, 100, 241–248.
30. Mauro, D., Biagioni, C., Pasero, M., Skogby, H., and Zaccarini, F. (2020) Redefinition of coquimbite,  $\text{AlFe}^{3+}_3(\text{SO}_4)_6(\text{H}_2\text{O})_{12} \cdot 6\text{H}_2\text{O}$ . *Mineralogical Magazine*, 84, 275–282.
31. MEPAG Next Decade Science Analysis Group. (2008) Science priorities for Mars sample return. *Astrobiology*, 8, 489–535.
32. Mills, S.J., Nestola, F., Kahlenberg, V., Christy, A.G., Hejny, C., and Redhammer, G.J. (2013) Looking for jarosite on Mars: The low-temperature crystal structure of jarosite. *American Mineralogist*, 98, 1966–1971.
33. Miura, H., Niida, K., and Hirama, T. (1994) Mikasaite,  $(\text{Fe}^{3+}, \text{Al})_2(\text{SO}_4)_3$ , a new ferric sulphate mineral from Mikasa city, Hokkaido, Japan. *Mineralogical Magazine*, 58, 649–653.
34. Rigaku (2014). PDXL 2, Rigaku powder diffraction data analysis software version 2.2. Rigaku Corporation, Tokyo, Japan.
35. Tosca, N.J., Agee, C.B., Cockell, C.S., Glavin, D.P., Hutzler, A., Marty, B., McCubbin, F.M., Regberg, A.B., Velbel, M.A., Kminek, G. and others. (2022) Time-sensitive aspects of Mars Sample Return (MSR) science. *Astrobiology*, 22, S-81–S-111.
36. Trueblood, K.N., Bürgi, H.-B., Burzlaff, H., Dunitz, J.D., Gramaccioli, C.M., Schulz, H.H., Shmueli, U., and Abrahams, S.C. (1996) Atomic displacement parameter nomenclature.

Report of a subcommittee on atomic displacement parameter nomenclature. *Acta Crystallographica*, A52, 770–781.

37. Wang, A., and Ling, Z.C. (2011) Ferric sulfates on Mars: A combined mission data analysis of salty soils at Gusev crater and laboratory experimental investigations. *Journal of Geophysical Research: Planets*, 116, E00F17.
38. Wang, A., Ling, Z., Freeman, J.J., and Kong, W. (2012) Stability field and phase transition pathways of hydrous ferric sulfates in the temperature range 50 °C to 5 °C: Implication for martian ferric sulfates. *Icarus*, 218, 622–643.
39. Wildner, M., Zakharov, B.A., Bogdanov, N.E., Talla, D., Boldyreva, E.V., and Miletich, R. (2022) Crystallography relevant to Mars and Galilean icy moons: crystal behavior of kieserite-type monohydrate sulfates at extraterrestrial conditions down to 15 K. *IUCrJ*, 9, 194–203.
40. Yang, Z., and Giester, G. (2018) Structure refinements of coquimbite and paracoquimbite from the Hongshan Cu–Au deposit, NW China. *European Journal of Mineralogy*, 30, 849–858.

### List of Figure captions:

**Figure 1.** A fragment of a studied sample from the Alcaparrosa mine with coquimbite (Coq), römerite (Röm) and aluminocopiapite (Acpi).

**Figure 2.** Evolution of the PXRD patterns as a function of temperature for coquimbite. The sequence of transformations (coquimbite→amorphisation→mikasaitite) is shown on the left.

**Figure 3.** TG and DSC curves for coquimbite. Coquimbite grains before the thermal analysis (left) and hematite grains obtained after heating (right).

**Figure 4.** General projection of the crystal structure of coquimbite (a,b).  $M1$ -centered octahedra are grey and  $M2$ -  $M3$ -centered octahedra are green;  $SO_4$  tetrahedra are yellow.  $[M_2M_3_2(SO_4)_6(H_2O)_6]^{3-}$  clusters and cyclohexane-like chairs are enlarged. Thermal expansion

tensor cross sections based on SCXRD data (c) with green indicating positive values and red indicating negative values.

**Figure 5.** Unit-cell dimensions of coquimbite in the temperature range from  $-173\text{ }^{\circ}\text{C}$  to  $77\text{ }^{\circ}\text{C}$  as obtained from the SCXRD data. The errors are smaller than the symbol size.

**Figure 6.** Coordination of  $M1$ ,  $M2$ ,  $M3$  and S sites with  $\Delta_d$  values labeled (a,b). Evolution of the selected bond length values in the range from  $-173\text{ }^{\circ}\text{C}$  (100 K) to  $-143\text{ }^{\circ}\text{C}$  (130 K) (stage I) and from  $-133\text{ }^{\circ}\text{C}$  (140 K) to  $77\text{ }^{\circ}\text{C}$  (350 K) (stage II) in  $M$ -centered octahedra and sulfate tetrahedra determined by LT- and HT-SCXRD. The dashed line indicates the boundary between Stage I and Stage II. The error bars are smaller than the size of markers.

**Figure 7.** O-H $\cdots$ O angular distortions in the structure of coquimbite upon temperature rise. The most significant angular changes are labeled.

**Figure 8.** (a) Temperature-dependent magnetic susceptibility of coquimbite measured in the applied fields of 0.01 T, 0.1 T, 1 T and 5 T. The inset shows inverse magnetic susceptibility of coquimbite measured in the applied fields of 0.01 T. The red line shows the fit obtained in accordance with  $S = 5/2$  trimer model with intratrimer interaction  $J = 2.4\text{ K}$ . (b) Field-dependent magnetization of coquimbite at 2 K, 10 K, 50 K and 100 K measured in static field. The red line shows the simulated  $M(H)$  curve that reaches saturation at  $M_s \sim 15.4\text{ }\mu\text{B/f.u.}$

**Figure 9.** (a) Temperature dependence of the specific heat  $C_p$  of coquimbite measured at zero field. The gray circles correspond to the raw data, the pink line represents the phonon contribution  $C_p^{ph}$  and the blue line is the magnetic contribution  $C_p^{magn}$  obtained by subtracting  $C_p^{ph}$  to  $C_p$ . (b)  $C_p^{magn}/T$  of coquimbite, as a function of temperature at 0 T and 9 T. (c) The calculated magnetic entropy  $S_{mag}$  as a function of temperature at 0 T and 9 T.

**Table 1.** Crystallographic data and refinement parameters for coquimbite at 100K, 200K, 300K and 350K. Parameters and refinement details for the entire temperature range are given in the supplemented cif file and deposited in the CCDC database (deposition numbers 2420549-2420574).

<b>Crystal data</b>				
Crystal system, space group	Trigonal, $P\bar{3}c$			
Temperature (K)	100	200	300	350
$a, c$ (Å)	10.8904(3), 17.0731(4)	10.9007(3), 17.0839(5)	10.9231(3), 17.0839(5)	10.9387(3), 17.0817(5)
$V$ (Å <sup>3</sup> )	1753.61(10)	1758.03(11)	1765.27(10)	1770.08(11)
$Z$	2			
Radiation type	Mo $K\alpha$			
$\mu$ (mm <sup>-1</sup> )	1.74	1.74	1.73	1.73
Crystal size (mm)	0.14 × 0.12 × 0.09			
<b>Data collection</b>				
Diffractometer	XtaLAB Synergy, Single source at home/near, HyPix			
Absorption correction	Multi-scan, <i>CrysAlis PRO</i> 1.171.41.104a			
$T_{\min}, T_{\max}$	0.609, 1.000	0.727, 1.000	0.867, 1.000	0.682, 1.000
No. of measured, independent and observed [ $I > 2\sigma(I)$ ] reflections	9876, 1428, 1327	10101, 1428, 1291	10064, 1435, 1322	9883, 1437, 1330
$R_{\text{int}}$	0.029	0.033	0.029	0.026
$(\sin \theta/\lambda)_{\max}$ (Å <sup>-1</sup> )	0.660	0.660	0.660	0.660
<b>Refinement</b>				
$R[F^2 > 2\sigma(F^2)], wR(F^2), S$	0.024, 0.067, 1.07	0.026, 0.072, 1.07	0.024, 0.067, 1.05	0.024, 0.067, 1.03
No. of reflections	1428	1428	1435	1437
No. of parameters	111	111	111	111
H-atom treatment	All H-atom parameters refined			
$\Delta\rho_{\max}, \Delta\rho_{\min}$ (e Å <sup>-3</sup> )	0.78, -0.48	0.89, -0.42	0.87, -0.42	0.71, -0.39

**Table 2.** Al/Fe ratio in M1 site in coquimbite samples from different localities and synthetic samples.

<i>M1 (2b) s.o.f.</i>	Reference
(Al <sub>0.63</sub> Fe <sub>0.37</sub> )	Giacovazzo et al. 1970
(Al <sub>0.66</sub> Fe <sub>0.34</sub> )	Yang and Giester 2018
(Al <sub>0.76</sub> Fe <sub>0.24</sub> )	Demartin et al. 2010
(Al <sub>0.90</sub> Fe <sub>0.10</sub> )	Fang and Robinson 1970
(Al <sub>0.91</sub> Fe <sub>0.09</sub> )	Majzlan et al. 2006
(Al <sub>0.93</sub> Fe <sub>0.07</sub> )	this work
(Al <sub>0.95</sub> Fe <sub>0.05</sub> )	Mauro et al. 2020
Al <sub>1.00</sub>	Majzlan et al. 2010

**Table 3.** Evolution of  $d(\mathbf{D}\cdots\mathbf{A})$  bond lengths and  $\langle\mathbf{DHA}\rangle$  angles in the temperature range 100 K – 350 K.  $\langle\mathbf{DHA}\rangle$  angles that change with increasing temperature by  $\geq 5^\circ$  are highlighted in bold.

$\mathbf{D-H}\cdots\mathbf{A}$	$d(\mathbf{D}\cdots\mathbf{A})$ and angle $\mathbf{D-H}\cdots\mathbf{A}$						$\Delta$ 350K– 100K
	100 K	150 K	200 K	250 K	300 K	350 K	

<b><i>H<sub>2</sub>O in isolated M1(H<sub>2</sub>O)<sub>6</sub> octahedra</i></b>							
<i>Ow1–H1…O2</i>	2.6900(17) 172(3)	2.6914(19) 170(4)	2.6935(19) 170(3)	2.6960(19) 170(3)	2.6982(18) 171(3)	2.6963(17) 174(3)	0.006 2
<i>Ow1–H2…O1</i>	2.6434(17) <b>170(3)</b>	2.6429(18) <b>173(3)</b>	2.6472(19) <b>171(3)</b>	2.6491(18) <b>170(3)</b>	2.6538(17) <b>169(2)</b>	2.6591(16) <b>162(3)</b>	0.016 –8
<b><i>H<sub>2</sub>O in cyclohexane-like arrangement</i></b>							
<i>Ow2–H3…O2</i>	2.7431(18) <b>158(3)</b>	2.739(2) <b>159(3)</b>	2.742(2) <b>157(3)</b>	2.741(2) <b>154(3)</b>	2.746(2) <b>157(3)</b>	2.746(2) <b>148(3)</b>	0.003 –10
<i>Ow2– H4a…Ow2</i>	2.732(3) <b>162(4)</b>	2.735(3) <b>160(4)</b>	2.737(3) <b>162(6)</b>	2.740(3) <b>162(5)</b>	2.743(3) <b>167(5)</b>	2.750(4) <b>170(5)</b>	0.018 8
<i>Ow2– H4b…Ow2</i>	2.724(3) 162(5)	2.727(3) 166(6)	2.730(3) 159(7)	2.736(4) 165(7)	2.737(3) 165(6)	2.738(3) 161(5)	0.014 –1
<b><i>H<sub>2</sub>O in [M<sub>2</sub>M<sub>3</sub><sub>2</sub>(SO<sub>4</sub>)<sub>6</sub>(H<sub>2</sub>O)<sub>6</sub>]<sup>3–</sup> clusters</i></b>							
<i>Ow3–H5…O1</i>	2.6599(18) <b>167(3)</b>	2.6591(19) <b>168(3)</b>	2.659(2) <b>168(3)</b>	2.6616(19) <b>167(3)</b>	2.6608(18) <b>169(3)</b>	2.6655(19) <b>176(3)</b>	0.006 9
<i>Ow3–H6…Ow2</i>	2.6424(18) 175(3)	2.644(2) 172(3)	2.644(2) 174(3)	2.645(2) 173(3)	2.646(2) 175(3)	2.647(2) 176(3)	0.005 1

**Figures:**

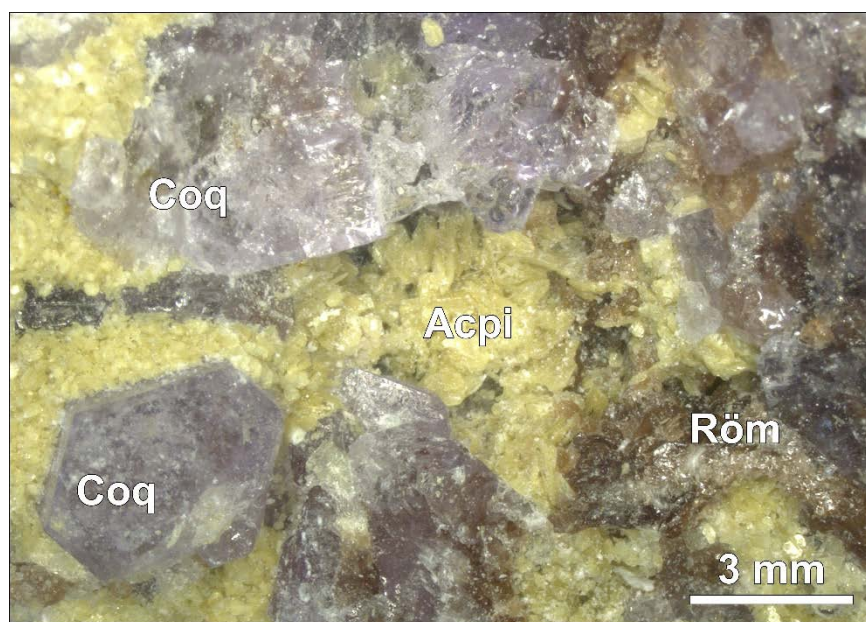


**Figure 1.** A fragment of a studied sample from the Alcaparrosa mine with coquimbite (Coq), römerite (Röm) and aluminocopiapite (Acpi).

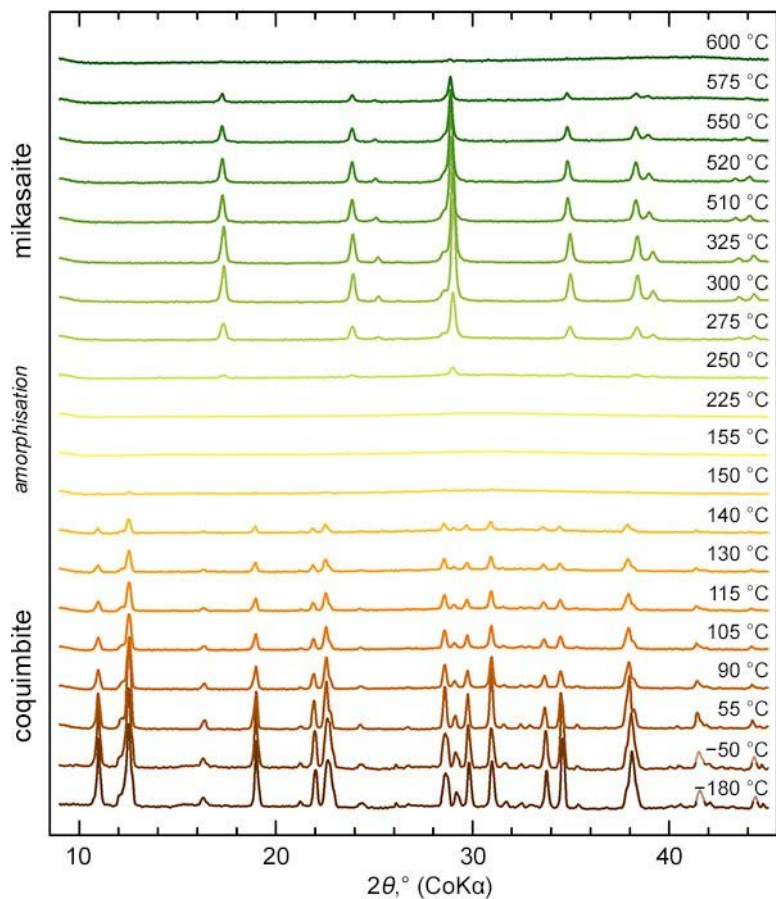


**Figure 2.** Evolution of the PXRD patterns as a function of temperature for coquimbite. The sequence of transformations (coquimbite→amorphisation→mikasaite) is shown on the left.

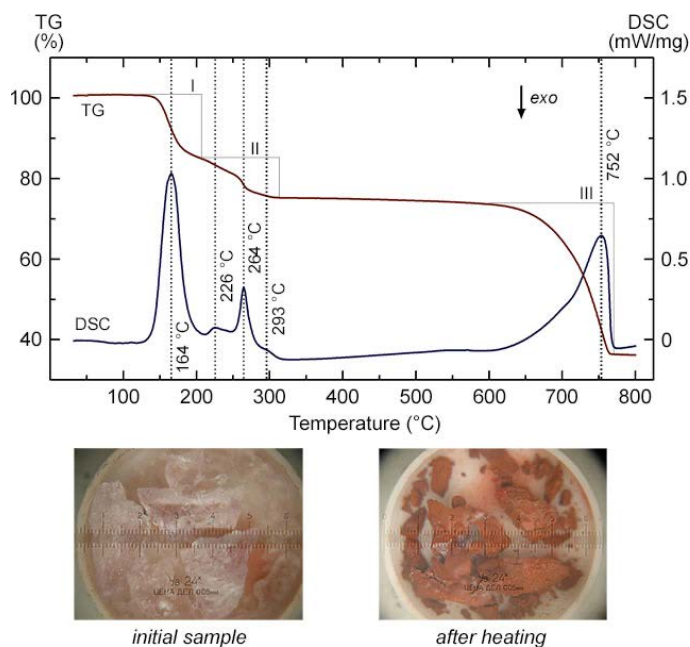


**Figure 3.** TG and DSC curves for coquimbite. Coquimbite grains before the thermal analysis (left) and hematite grains obtained after heating (right).

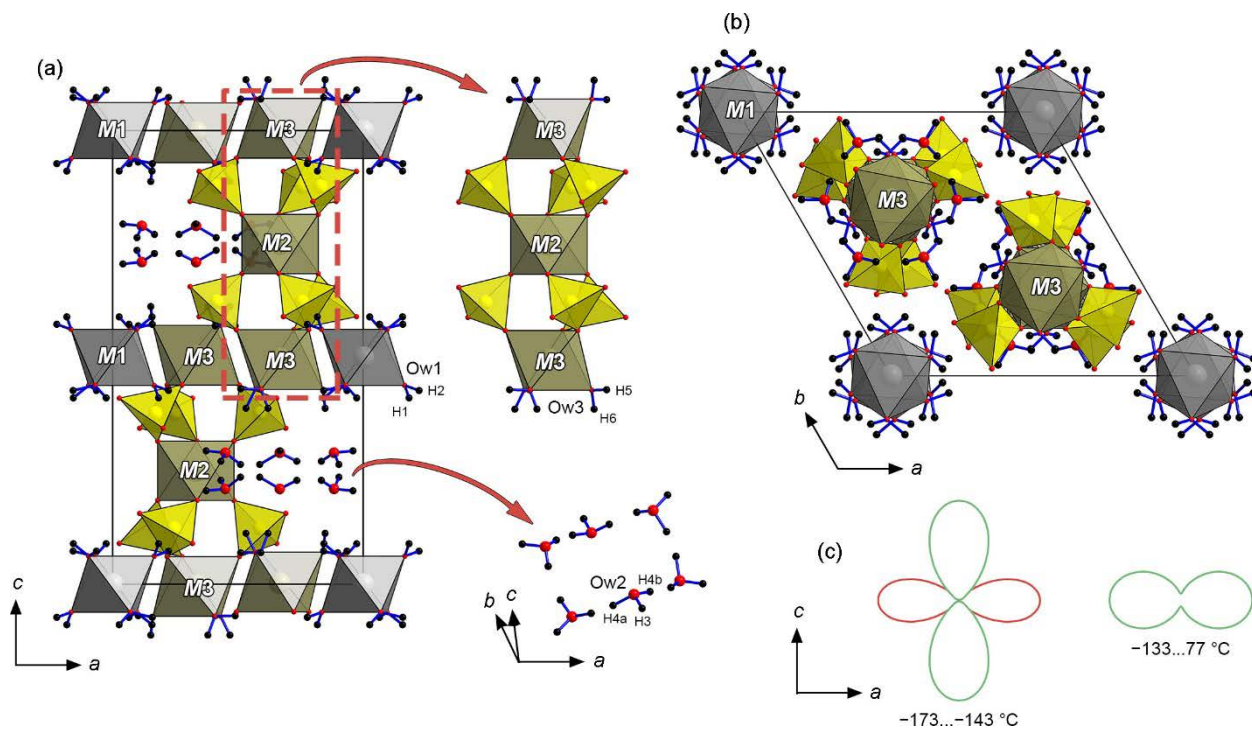


**Figure 4.** General projection of the crystal structure of coquimbite (a,b). *M1*-centered octahedra are grey and *M2*- *M3*-centered octahedra are green; SO<sub>4</sub> tetrahedra are yellow. [M<sub>2</sub>M<sub>3</sub><sub>2</sub>(SO<sub>4</sub>)<sub>6</sub>(H<sub>2</sub>O)<sub>6</sub>]<sup>3-</sup> clusters and cyclohexane-like chairs are enlarged. Thermal expansion tensor cross sections based on SCXRD data (c) with green indicating positive values and red indicating negative values.

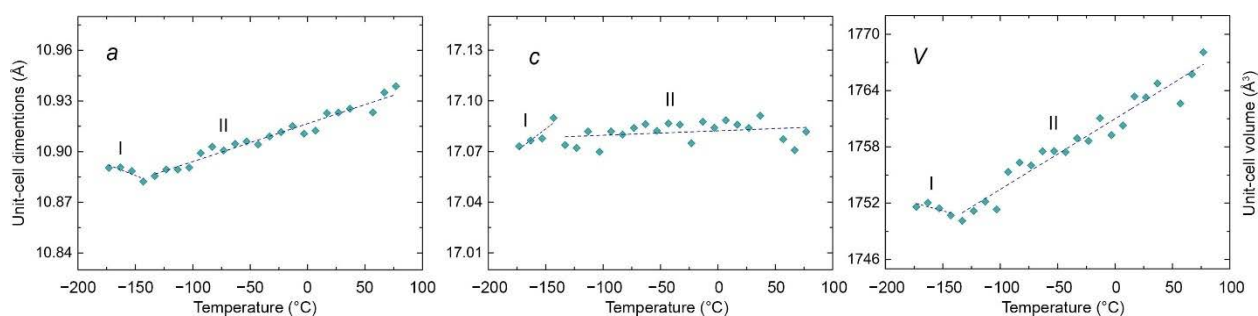


**Figure 5.** Unit-cell dimensions of coquimbite in the temperature range from -173 °C to 77 °C as obtained from the SCXRD data. The errors are smaller than the symbol size.

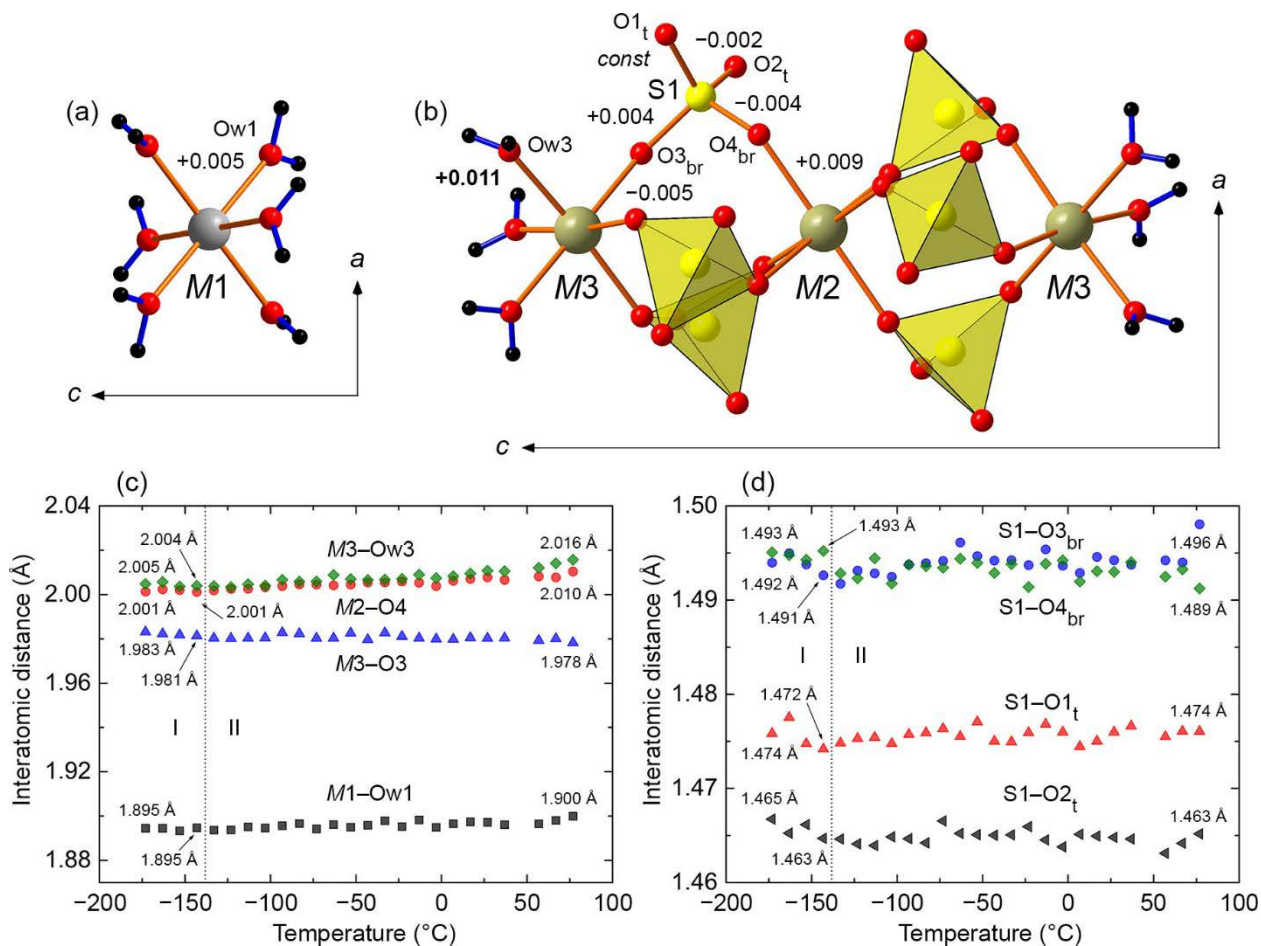


**Figure 6.** Coordination of  $M1$ ,  $M2$ ,  $M3$  and S sites with  $\Delta_d$  values labeled (a,b). Evolution of the selected bond length values in the range from  $-173$  °C (100 K) to  $-143$  °C (130 K) (stage I) and from  $-133$  °C (140 K) to  $77$  °C (350 K) (stage II) in  $M$ -centered octahedra and sulfate tetrahedra determined by LT- and HT-SCXRD. The dashed line indicates the boundary between Stage I and Stage II. The error bars are smaller than the size of markers.

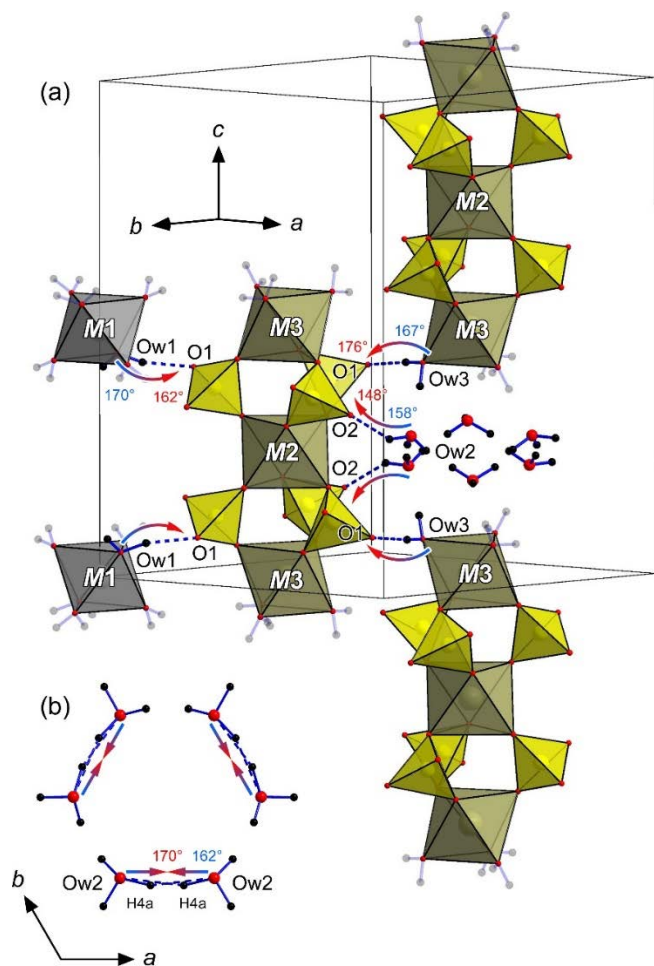


**Figure 7.** O-H...O angular distortions in the structure of coquimbite upon temperature rise.

The most significant angular changes are labeled.

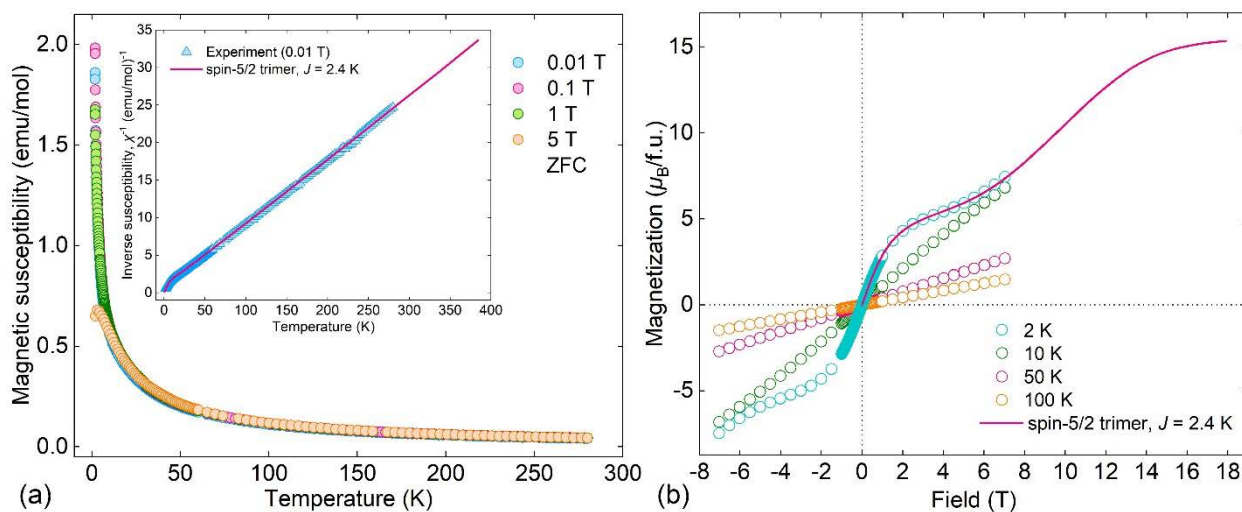


**Figure 8.** (a) Temperature-dependent magnetic susceptibility of coquimbite measured in the applied fields of 0.01 T, 0.1 T, 1 T and 5 T. The inset shows inverse magnetic susceptibility of coquimbite measured in the applied fields of 0.01 T. The red line shows the fit obtained in accordance with  $S = 5/2$  trimer model with intratrimer interaction  $J = 2.4$  K. (b) Field-dependent magnetization of coquimbite at 2 K, 10 K, 50 K and 100 K measured in static field. The red line shows the simulated  $M(H)$  curve that reaches saturation at  $M_s \sim 15.4 \mu_B/\text{f.u.}$

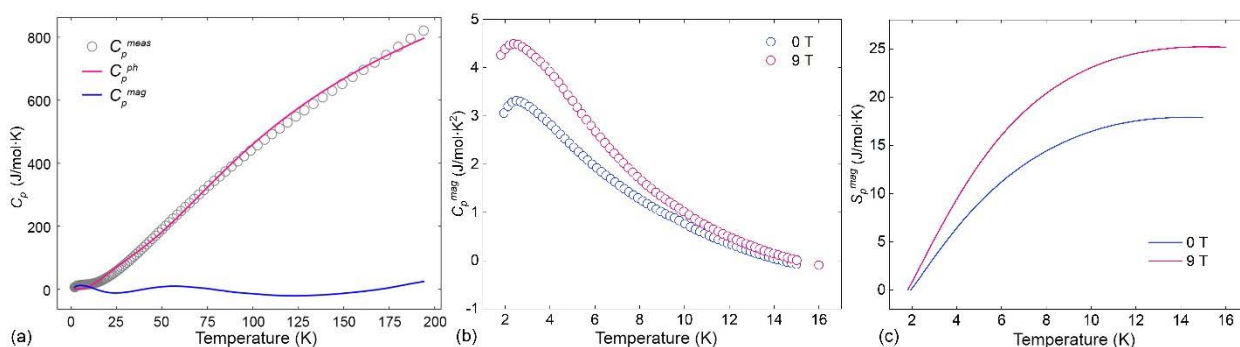


**Figure 9.** (a) Temperature dependence of the specific heat  $C_p$  of coquimbite measured at zero field. The gray circles correspond to the raw data, the pink line represents the phonon contribution  $C_p^{ph}$  and the blue line is the magnetic contribution  $C_p^{mag}$  obtained by subtracting  $C_p^{ph}$  to  $C_p$ . (b)  $C_p^{mag}/T$  of coquimbite, as a function of temperature at 0 T and 9 T. (c) The calculated magnetic entropy  $S_{mag}$  as a function of temperature at 0 T and 9 T.